Nocturnal camouflage through background matching against moonlight

Juan J. Negro[a,1] ID, Salvador Bará[b] ID, David Galadí-Enríquez[c] ID, Juan Luis Nieves[d] ID, Miguel A. Martínez-Domingo[d] ID, Alejandro Ferrero[e] ID, Joaquín Campos[e] ID, Carmen Bao-Varela[f] ID, Eduard Masana[g,h,i] ID, and Carlos Camacho[a,1] ID

Affiliations are included on p. 10.

Camouflage is often considered a daytime phenomenon based on light and shade. Nocturnal camouflage can also occur, but its mechanistic basis remains unclear. Here, we analyze the conditions for background matching (BM) of avian predators against the night sky. Such concealment is achieved when the contrast between the predator and the sky is smaller than the contrast detection threshold of prey. This condition cannot be fulfilled under isotropic skies, as in fully overcast or moonless nights. However, on clear moonlit nights, the isotropy of the sky radiance is broken due to the presence of the Moon, and the conditions for BM can be met for a wide range of sky directions. This effect is mainly dependent on the altitude of the Moon above the horizon, rather than on Moon phase. We have modeled the feasibility of concealment through BM of a typically white barn owl (*Tyto alba*) when hunting rodents, based on its contrast against the moonlit sky. We considered the radiometric quantities of the sky, the ground, and the bird's undersides. Our results show that a barn owl with highly reflecting underparts may approach a rodent from broad regions of the moonlit sky while keeping itself below the contrast detection threshold of the mouse M-cones and rods. S-cones, in turn, remain below their excitation threshold for most of the lunar cycle. Our results demonstrate that the white color of barn owls serves as camouflage tailored to the moonlit sky background, providing a mechanistic basis for understanding nocturnal camouflage.

phenotype-time correlations | Posch ratio | moon | avian predators | barn owl

Since the pioneering works of Thayer (1) on camouflage and crypsis more than a century ago, considerable research effort has been directed toward understanding the adaptive functions of animal coloration (2, 3), including signaling (4, 5), thermoregulation (6), and concealment in both terrestrial and aquatic environments (7).

Avoiding visual detection is one of the functions of the integument, including bird plumages and mammal coats, conferring advantages to both predators and prey. Several basic mechanisms have been proposed to reduce the detectability of an individual within the visual field of the receiver, including self-shadow concealing (SSC) and background matching (BM) (7). SSC acts by reducing the monocular depth clues, making it more difficult the perception of the three-dimensional shape of the object that is used to separate objects from their background (8). BM acts by canceling out the Weber contrast of the individual against the surrounding background. It has been hypothesized that the widely different spectral reflectances of the dorsal and ventral parts of the bodies of many species are instrumental in enabling SSC, BM, or both.

Several works have pointed out that BM against the sky might not be perfectly attainable under natural light illumination due to the highly variable photic environment and, more decisively, to the typically large imbalance between downward and upward radiances, particularly in aquatic environments (9, 10). As a matter of fact, when the radiance incident on an object is equal to or smaller than the radiance of the background, the conditions for contrast cancellation cannot generally be met, because the object reflectance cannot surpass the value of unity and the object therefore looks darker than the background. This is the situation commonly experienced under nearly isotropic skies (e.g. fully overcast, or clear moonless starry nights) as well as in media with intense multiple scattering (e.g. dense fog, or aquatic environments). In such cases, an additional contribution of light (e.g. through bioluminescence) is needed to increase the radiance from the object and thus fulfill BM conditions (11).

However, when the Sun or the Moon is present above the horizon, the isotropy of the illuminant is broken and this gives rise to drastic changes in the visual landscape: On the one hand, the radiance from different sky directions may vary across several orders of magnitude, providing backgrounds with very different brightness (see, e.g., refs. 12–17), and,

Significance

Predators need to approach their prey undetected. Barn owls (*Tyto alba*) differ from the patterned designs of most nocturnal birds in having white underparts. Modeling radiometric quantities of the sky, the ground, and the barn owl itself, we provide evidence that this predator becomes invisible to ground-dwelling rodents under most moonlit skies. Paradoxically, a white owl minimizes detection by rodent prey located on the ground when approaching them from above under bright moonlight. The mechanism we describe is distinct from the current interpretation that barn owls are highly visible to their rodent prey and freeze them in fear. Our results provide insights into the role of the plumage spectral reflectance on hunting efficacy at night.

[1]To whom correspondence may be addressed. Email: negro@ebd.csic.es or ccamacho@ebd.csic.es.

on the other hand, the upward radiance is highly increased due to the ground reflection of the direct Sun or Moon illumination. Both effects acting together open up the possibility of achieving the required BM balance. Despite its potential role in BM, the angular distribution of environmental light under these circumstances has received little attention in camouflage studies (but see refs. 18–20).

Here we use a nocturnal avian predator as a model to show that strongly anisotropic skies, typical of clear sunny days and moonlit nights, provide the required conditions for enabling the predator to conceal itself through BM and thus avoid being detected by prey located on the ground. Besides abiotic factors, such as the position of the Moon on the sky, the reflectance properties of the terrain, and the state of the atmosphere (e.g. aerosol content), an in-depth analysis of this issue requires consideration of some aspects of the predator–prey system, including the plumage characteristics of the predator, its overall coloration, the visual system of the prey, and the predator's diet and foraging mode. The barn owl (*Tyto alba*) has white ventral areas, as well as a white facial disk, and therefore its overall appearance differs from the highly patterned melanized plumage of all other members of the Strigiformes (6), except *Bubo scandiacus*, a species that occupies arctic tundra environments. Barn owls typically forage in open areas, often in urban or agricultural landscapes (21). In addition, they are unique among owls in their foraging mode and angle of attack in the final approach to the prey: While most owl species hunt by diving obliquely from a perch to the ground, barn owls typically hunt by flying and hovering and finally diving vertically to the ground [(22); *SI Appendix*, Fig. S1].

Barn owls are polymorphic in plumage color, varying from pure white to rufous in the ventral parts. The reddish color is due to variable contents of pheomelanin pigments (23). It has recently been shown that red owls are less successful than white owls at capturing rodent prey on moonlit nights, resulting in differential fitness effects of moon phase on each color morph (24). Color-dependent effects of moon phase are hypothesized to reflect an advantage for the whitest olws under full-moon conditions because bright moonlight makes them more conspicuous to rodents and induces longer freezing times, facilitating their capture (24). This hypothesis is based on the assumption that a white ventral plumage is brightly perceived by their prey, which somehow do not react. Other authors also assumed that a white plumage increases conspicuousness against a dark background (25). We offer additional insights into this topic and, in fact, propose a different hypothesis, that on nights when the Moon is above the horizon the whitest owls are more difficult to detect than more melanized ones because their white plumage better matches the background of the moonlit sky given the visual system of their rodent prey. Barn owls are known to hunt prey by hearing, and also for being themselves silent flyers (e.g., ref. 26). Concealment (this study) and conspicuousness (24) as mechanisms contributing to predation are substantially different from each other and may even seem contradictory, but they are not necessarily so. While it would be contradictory that barn owls did their best to avoid being detected visually and by sound while showing themselves bright and conspicuous at the same time, both strategies could be synergistically used as long as they operate in nonoverlapping segments of the flight path (e.g., initial approach and final strike).

Our approach consists of four sequential steps: i) an assessment of the structural components of the nocturnal light environment and a formalization of the isomorphic relationship between moonlit nightscapes and their daytime sunlit counterparts; ii) a calculation of the conditions for BM in terms of the Posch ratio of the sky light (i.e. the ratio of the global horizontal irradiance to the direction-dependent sky radiance; see refs. 27–29); iii) an estimation of both the conditions for BM in the photoreceptor passbands of the prey and of the maximum distances at which the predator may be visually detected based on the general properties of the contrast sensitivity functions (CSF) of the prey; and iv) an integrated assessment of the feasibility of nocturnal camouflage of barn owls through BM.

Results

Modeling BM Under Moonlight.

The structure of the nocturnal landscape. Humans tend to perceive the natural night as a rather dark and uninformative environment. However, this is not so for nocturnally adapted species (30–34). On moonless nights free from artificial light pollution, the visual nightscape in the optical region of the electromagnetic spectrum is dominated by the brightness of the starry sky and its reflections on the ground. The radiance of the starry sky can be efficiently modeled in any retinal photoreceptor spectral band ((35, 36); see example in *SI Appendix,* Fig. S2). The Moon is the main source of natural light at night in pristine areas. The horizontal illuminance of a full Moon may reach values of ~0.3 l ×, two orders of magnitude larger than the illuminance of the moonless sky. The spectral irradiance of moonlight at the upper layers of the terrestrial atmosphere, $E_M(\lambda;g)$, can be calculated using the Kieffer and Stone (37) ROLO model as:

$$E_M(\lambda;g) = \left(\frac{1\,\text{au}}{D_{SM}}\right)^2 \left(\frac{D_{MO}}{D_{MV}}\right)^2 \frac{\Omega_M}{\pi} A(\lambda;g) E_\odot(\lambda), \quad [1]$$

where $E_\odot(\lambda)$ is the extra-atmospheric Sun spectral irradiance, λ is the wavelength, g is the Moon signed phase angle ($g = 0°$ for Full Moon, $0° < g < 180°$ for the waning Moon, $g = 180°$ for New Moon, and $-180° < g < 0°$ for the waxing Moon), D_{SM} is the actual distance Sun-Moon measured in astronomical units of distance, au (1 au= 149 597 870.7 km), D_{MV} is the distance from the Moon to the observer in km, with $D_{MO} = 384\,400$ km, and $\Omega_M = 6.4177 \times 10^{-5}$ sr is the solid angle of the full Moon at nominal D_{MO} distance. $A(\lambda;g)$ is the ROLO disc-equivalent reflectance factor of the Moon (unitless), called "disk-equivalent albedo" in ref. 37.

To formalize our calculations, let us denote by $L(z, \varphi; z_s, \varphi_s; \lambda;g)$ the spectral radiance of the moonlit sky, as seen by a ground observer looking at an arbitrary direction oriented at angles z (zenith distance) and φ (azimuth) during phase g of the lunar cycle, when the Moon is located in the direction (z_s, φ_s) (for basic geometric and radiometric definitions see *SI Appendix*). For most directions on the sky this radiance is due to moonlight scattered by the terrestrial atmosphere. If the observer is looking directly at the position of the Moon on the sky $(z = z_s, \varphi = \varphi_s)$, then its strong direct radiance (only attenuated by propagation through the atmosphere) shall be added to the scattered radiance term. The resulting spectral radiance of the sky can be written as

$$L(z, \varphi; z_s, \varphi_s; \lambda;g) = \Psi(z, \varphi; z_s, \varphi_s; \lambda) E_M(\lambda;g), \quad [2]$$

where $\Psi(z, \varphi; z_s, \varphi_s; \lambda)$, is a function with units inverse sterradians (sr^{-1}) relating both radiometric quantities, irradiance, and radiance. This function depends on the relative angles of illumination (z_s, φ_s) and observation (z, φ), and on the molecular and aerosol optical properties of the atmosphere for each wavelength λ, but not on the amount of moonlight that reaches the upper layers of the atmosphere (see refs. 14, and 15). The direct radiance term can be calculated by applying the Lambert-Bouguer law of exponential

attenuation to the Moon extra-atmospheric irradiance, taking into account the Moon zenith angle and the vertical molecular and aerosol extinction profiles of the atmosphere. An online calculator of radiometric and photometric indicators of moonlight is available at https://gambons.fqa.ub.edu/moon.html). Moonlit nightscapes are nearly isomorphic to daytime landscapes. The function Ψ holds the key of the remarkable similarity between moonlit nightscapes and their daytime counterparts (see *SI Appendix*, Fig. S3A and "*Isomorphy of nocturnal and diurnal landscapes*").

A simplified model for narrow-band BM against the night sky. For simplicity, we refer here to the case of a predator located on the vertical of its prey (Fig. 1), although the results can be immediately applied to predators seen against any arbitrary direction (z, φ) in the sky hemisphere. From a formal standpoint, BM equations are strictly valid only if the radiometric quantities displayed in Fig. 1 are interpreted as spectral densities, that is, as spectral radiance, irradiance, and reflectance. They apply separately to each elementary spectral interval. However, all equations are approximately valid for the practically interesting case of the photon flux captured by narrow-band retinal photoreceptors (bandwidth $\lesssim$ 100 nm), a taxonomically widespread trait, and for their associated contrasts. In this sense, the formulation here is a simplified but insightful BM model The rigorous BM model for arbitrary photoreceptor bandpass, including potential fluorescent reemission by the predator, is developed in *SI Appendix* under "*Full spectral model for in-band BM*", and is used for computing the numerical results shown in the case study below.

The sky radiance in an arbitrary direction is denoted by $L(z, \varphi)$. L_0 stands for the zenith radiance, i.e. $L_0 = L(0^\circ, 0^\circ)$. E_g^- is the irradiance incident on ground, calculated according to *SI Appendix*, Eq. S11. Assuming a Lambertian reflection on the ground –i.e., ground reflectance factor ρ_g independent of the illumination and reflection directions– the radiance L_g^+ reflected from the ground for any direction is given by *SI Appendix*, Eq. S16 for any direction. The radiance from all points on the ground propagates to the ventral side of the avian predator, whose reflectance can be assumed Lambertian and is described by its reflectance factor ρ_a^-, producing a downward radiance L_a^-. The irradiance on the dorsal, upward-facing side of the predator is for all practical purposes equal to the irradiance incident on ground, if its flight altitude above ground level does not exceed a few hundred meters. This irradiation gets reflected on the avian dorsal side, assumed Lambertian and with a
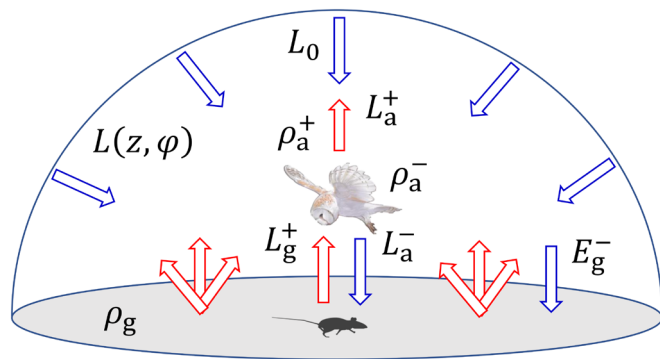
reflectance factor ρ_a^+, and gives rise to a reflected upward radiance L_a^+.

Under these assumptions, the conditions for perfect BM can be easily derived for each elementary spectral interval. The Weber contrast between the predator and the immediate surrounding sky is:

$$\gamma_W = \frac{L_a^- - L_0}{L_0} = \frac{L_a^-}{L_0} - 1. \quad [3]$$

BM of the predator against the zenith sky occurs when the Weber contrast of the predator's ventral side cancels out ($\gamma_W = 0$), a condition equivalent to equating the radiances $L_a^- = L_0$.

By repeated application of *SI Appendix*, Eq. S16 to the relevant radiometric quantities, the value of L_a^- can be derived in terms of E_g^-. The individual steps of this calculation are $L_g^+ = \left(\rho_g/\pi\right)E_g^-$, $E_a^+ = \pi L_g^+$ (irradiance incident on the ventral side of the predator, due to the Lambertian radiance from the whole ground plane), and $L_a^- = \left(\rho_a^-/\pi\right)E_a^+ = \left(\rho_a^- \rho_g/\pi\right)E_g^-$. The Weber contrast is then:

$$\gamma_W = \frac{\rho_a^- \rho_g E_g^-}{\pi L_0} - 1, \quad [4]$$

and the condition for zenith BM becomes:

$$\left(\rho_a^- \rho_g/\pi\right)\left(E_g^-/L_0\right) = 1. \quad [5]$$

The factor E_g^-/L_0 is the ratio of the ground irradiance produced by the hemispherical radiance distribution $L(z, \varphi)$ to the value of the radiance at the zenith, L_0. This quotient, with units sr, is a particular instance of a Posch ratio (see refs. 27–29). In terms of the zenith Posch ratio $P_0 = E_g^-/L_0$ the condition for BM against the zenith sky is finally given by:

$$P_0 = \frac{\pi}{\rho_a^- \rho_g}. \quad [6]$$

Eq. 6 shows that narrow-band BM can be achieved if the sky radiance distribution surrounding the object (including all light sources mentioned above) is such that its Posch ratio E_g^-/L_0 equals $\pi/\rho_a^- \rho_g$. To get some insight about the order of magnitude of the quantities involved in this calculation, let us notice that for typical reflectance factors of the ground ($\rho_g \sim 0.1 - 0.2$) and highly reflecting objects ($\rho_a^- \sim 0.5$), perfect BM could be achieved if $E_g^-/L_0 \sim 30 - 60\,$sr. It has been widely accepted that this is seldom attainable in practice due to the assumed large difference between the downward and upward radiant flux in nonurbanized areas of our planet. This argument, however, overlooks some key directional effects of the illumination provided by the Sun or the Moon when they are shining above the local horizon. It is true that in conditions of nearly equal radiance arriving from all upward hemisphere directions, $L(z, \phi) \approx L_0$, e.g. under overcast skies or in the midst of a dense fog, the Posch ratio is $P_0 = E_g^-/L_0 \approx \pi$, and hence according to Eq. 6 fulfilling BM conditions would require $\rho_a^- \rho_g \approx 1$, implying a clearly unrealistic perfectly diffuse reflectance from both ground and predator. However, when the Sun or the Moon are present on the clear sky, the irradiance E_g^- on the ground can be much larger than π times the radiance of the region of the sky against which the predator is seen (in our present example, the radiance at the zenith, L_0). In these conditions, very large values

Fig. 1. Radiometric quantities for analyzing camouflage of an avian predator through BM against the sky, as seen from a prey on the ground. $L(z, \phi)$, sky radiance from the direction defined by the zenith angle z and azimuth ϕ; L_0, zenith sky radiance; E_g^-, irradiance incident on ground; ρ_g, ground reflectance factor; L_g^+, ground reflected upward radiance; ρ_a^-, avian ventral reflectance factor; L_a^-, avian reflected downward radiance; ρ_a^+, avian dorsal reflectance factor; L_a^+, avian reflected upward radiance (see text for details).

of P_0 allowing to fulfill the BM condition in Eq. **6** can be actually experienced (*SI Appendix*, Fig. S5).

Note that Eqs. **4**–**6** can be applied to predator locations other than the zenith by just replacing in these formulae L_0 by $L(z, \phi)$, and P_0 by $P(z, \phi) = E_g^- / L(z, \phi)$. Details on the general properties of the Posch ratios, the full spectral model for in-band BM, CSF, and estimated maximum detection distance are in *SI Appendix*.

As a final remark, camouflage of a predator against the sky, as seen from ground, is more difficult to achieve than camouflage of a prey against the surrounding substrate, as seen from above, since the latter case only requires matching the spectral reflectances of prey, ρ_p^+, and ground ($\rho_p^+ = \rho_g^+$). When this is achieved, camouflage becomes independent from the illumination conditions. A very interesting set of observations of this match in the nocturnal environment in marine shallow waters (2 to 5 m depth) can be found in ref. 31.

Feasibility of BM Against the Moonlit Sky in Prey Photoreceptor Bands: A Case Study.
The analysis of the role of BM in the predator–prey interaction system formed by barn owls and rodents is based on the CSF and estimates of maximum detection distance given in *SI Appendix*. Our goal is to get basic insights about the order of magnitude of the involved effects. Evaluating the feasibility of BM in this predator–prey system requires i) a fully spectral model of the radiance of the moonlit sky, ii) field data of the terrain spectral reflectance, iii) empirical data on the angular and spectral properties of the light reflected by the barn owl plumage, and iv) a model of rodent vision, including the shape and values of the appropriate CSF functions.

Sun and Moon extra-atmospheric spectral irradiances and radiance of the moonlit sky.
For calculating the Moon irradiance $E_M(\lambda; g)$ in Eq. **1** we used the extra-atmospheric Sun irradiance spectrum $E \odot (\lambda)$ *sun_reference_STIS_002* from the CALSPEC database (38, 39). The original irradiance data in energy units erg·s^{-1}·cm^{-2}·Å^{-1} were first transformed to J·s^{-1}·m^{-2}·nm^{-1}, and subsequently to photons·s^{-1}·m^{-2}·nm^{-1} (*SI Appendix*, Fig. 6S) by multiplying the energy spectra by λ/hc, the inverse of the photon energies, where λ is the wavelength (in m), $h = 6.62607015 \times 10^{-34}$ J·s is the Planck constant, and $c = 2.99792458 \times 10^8$ m·s^{-1} is the speed of light in vacuum (40).

The effective Moon reflectance factor $A(\lambda; g)$ was obtained for each Moon phase from the ROLO coefficients tabulated for a discrete set of wavelengths and equation 10 of ref. 37. Note that in their equation the variable g is the absolute value of the phase, not the signed one. The resulting reflectance factor was interpolated in a more closely spaced set of wavelengths, and subsequently smoothed to match the overall shape of a linearly transformed version of the reflectance spectrum of a mix of *Apollo* lunar soil samples (figure 8 of ref. 37). The smoothed values were further corrected by taking into account refs. 41–43. Several $A(\lambda; g)$ curves for different Moon phase angles are shown in *SI Appendix*, Fig. S3. Note that these curves have similar shapes, and that their values depend strongly on g because $A(\lambda; g)$ includes the effect of the changing angular size of the Moon illuminated fraction.

From $A(\lambda; g)$ the Moon irradiance $E_M(\lambda; g)$ is obtained using Eq. **1**, and the all-sky radiance and derived photometric quantities are then calculated using Eq. **2**. The atmospheric PSF $\Psi(z, \varphi; z_s, \varphi_s; \lambda)$ in Eq. **2** is composed of two terms, one accounting for the scattered light and other for the direct radiance. The scattered light term is given by the factor multiplying the irradiance $F_S(\lambda)$ in equation 18 of ref. 15, applied here separately to each individual wavelength. The parameters chosen are as follows:

The airmass number was calculated using the expression by ref. 44, $M(z) = 1/\left[\cos z + 0.50572 \cdot (96.07995 - z)^{-1.6364}\right]$, with the zenith angles z expressed in degrees. The molecular optical depth of the atmosphere at different wavelengths was calculated according to ref. 45 as $\tau_R(\lambda) = 0.00879\lambda^{-4.09}$, with λ expressed in micron. The aerosol optical depth of the atmosphere $\tau_A(\lambda)$ and the aerosol properties (Henyey-Greenstein asymmetry parameter and albedo) were specified at $\lambda_0 = 550$ nm, and their spectral dependence evaluated according to Eqs. **6**–**8** respectively, of ref. 46, with Angström power law scattering and absorption exponents equal to 1.0. The direct radiance term of the PSF in Eq. **2**, in turn, is given by the exponential Lambert-Beer's law describing atmospheric attenuation along the direct light path, divided by the solid angle subtended by the illuminated fraction of the Moon at each phase angle and distance to the Earth (see *SI Appendix*, Fig. S7 for typical values of the horizontal illuminance and average hemispheric luminance of moonlight for different Moon altitude angles).

Ground spectral reflectance.
The reflectance of the soil plays an important role in any BM mechanism of avian predators against the surrounding sky, since it determines the fraction of downward sky radiation that will be reflected upward, acting as the source illuminating the avian ventral surfaces while on flight (*SI Appendix*, Fig. S8).

Optical properties of the barn owl plumage.
White plumages are highly reflective. This generally arises from incoherent scattering in disordered micro- or nanostructures with negligible absorption surrounded by air, as a result of multiple achromatic reflections (47). However, there are few published data on barn owl reflectance in the spectral region (300 to 700 nm), relevant for mice photoreception (see next subheading). For the purposes of this work, we took a set of measurements of three basic optical properties of a barn owl specimen from the scientific collection of the Estación Biológica de Doñana–CSIC ("*Material and Methods*").

The spectral reflectance of the barn owl tended to increase for longer wavelengths (Figs. 2 and 3), as reported for the white plumage patches of other Strigiformes (e.g., *Bubo bubo*; ref. 48).

Mice photoreceptors, absolute thresholds, and contrast detection thresholds.
Like most mammals, mice are dichromatic. Their cones express S- and M-opsins with peak sensitivities in the UV (360 nm) and VIS (508 nm), respectively, while their rodopsin peaks at 498 nm ((49, 50); *SI Appendix*, Fig. S6). Most cones express both opsins, with a retinal dorso-ventral gradient of increasing S-opsin and decreasing M-opsin; the relatively small fraction of cones expressing only the S-opsin ("true" S-cones) are concentrated in the ventral retina and are deemed instrumental for color discrimination in the upper visual field (51, 52). Rodent eye optics have characteristic features which determine the mapping between the radiance of the outside world and their retinal photoreceptor mosaic (53, 54). Rats have been shown to maintain a large region of binocular overlap directly overhead, robust against head movements (55), "almost certainly for the detection of overhead predators" (56).

Two aspects of the rodent visual system are of special interest for this work, namely the absolute detection thresholds (i.e. the minimum illumination levels required to elicit quantifiable visual responses), and the contrast detection thresholds, defined as the minimum contrast between an object and the background necessary for this object being successfully detected when photoreceptors are active. The values of these thresholds may vary depending on the type of photoreceptor and output metric. Thresholds can be measured for retinographic, optokinetic, optomotor, and behavioral responses, being the latter the most directly related to predator–prey dynamics.
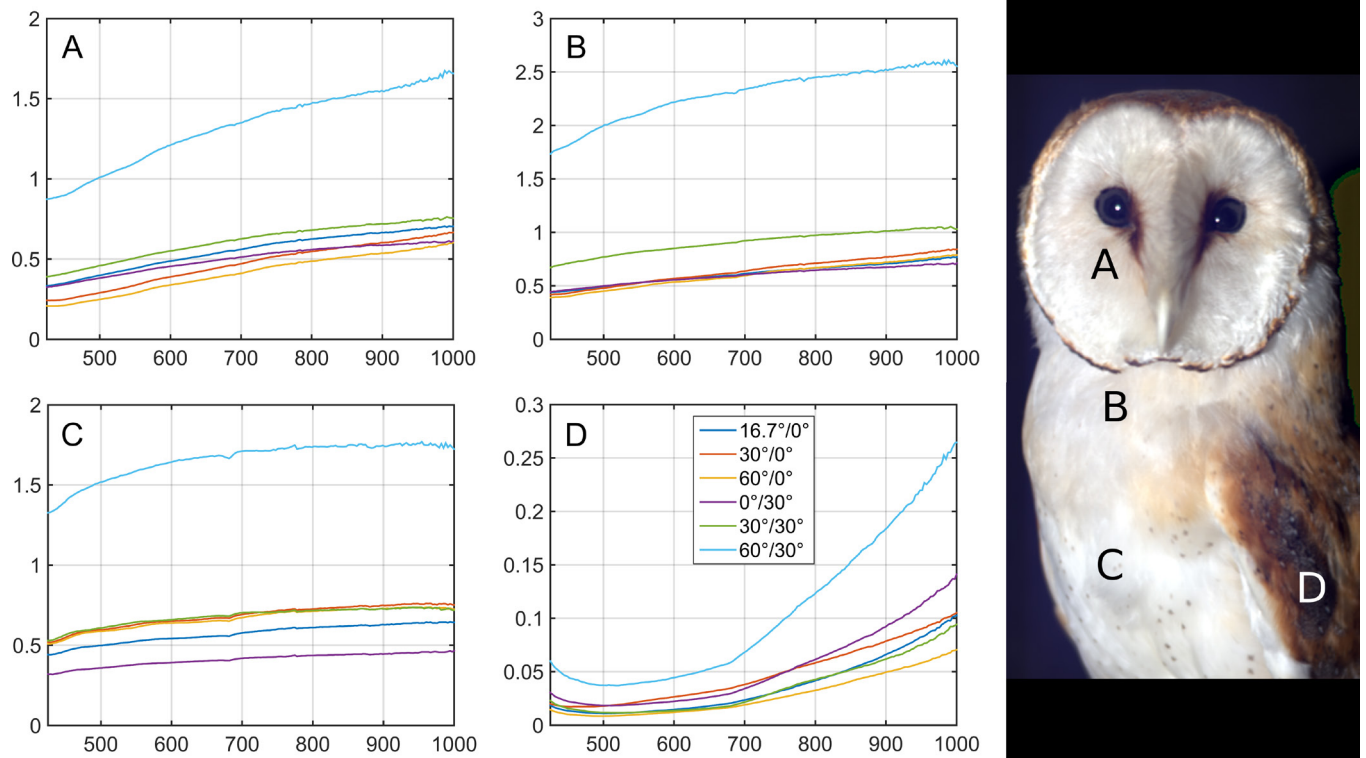
Fig. 2. *Vertical axes:* Reflectance factors of the barn owl specimen, from hyperspectral measurements made in the plumage areas indicated in the figure (*A–D*). *Horizontal axes:* wavelength (nm). Legends indicate the light source azimuth/altitude, both angles measured from the sagittal axis normal to the frontal plane of the specimen facial disk. Azimuths correspond to angles measured within the horizontal plane perpendicular to the barn owl image (transverse plane), altitudes to angles measured within the vertical plane perpendicular to it (sagittal plane). The barn owl image is a false Red-Green-Blue image rendered from the spectral reflectance image captured.

Absolute thresholds. The absolute luminance threshold for eliciting behavioral responses in mice is relatively low. The absolute, dark-adapted, luminance threshold of mice is estimated to be 11.2 μcd/m² (57). This threshold luminance is about 20 times smaller than the nominal clear sky zenith luminance in an average moonless starry night [200 μcd/m²; (58, 59)]. It is comparable to or five times lower than the 40 to 50 μcd/m² expected from a starlight-illuminated terrain with reflectance 0.2 to 0.25. The visual function of mice is then expected to perform efficiently under starlight in moonless nights and, consequently, under all levels of moonlight.

The specific thresholds for each type of photoreceptor are of interest to assess which of them is fully functional under moonlight. Mice luminance thresholds for rod and cone vision are roughly similar to humans (60). Analyzing the thresholds for optomotor responses in mice with normal vision, mice without functional cones, and mice without functional rods, (61) found that, for the spectral composition of the light source used in their experiment, rods are active for luminance from -6.0 to -2.0 log cd m^{-2}, and cones from -4.0 to $+2.0$ log cd m^{-2}, both being active in the mice mesopic range -4.0 to -2.0 log cd m^{-2} (for more details on absolute thresholds of M cones, S cones, and rods, see *SI Appendix*, Fig. S9).

CSF and maximum detection distance. Absolute thresholds are useful to determine whether or not a given photoreceptor channel is active under moonlight illumination. To determine the distance range at which mice may detect an approaching predator, additional visual metrics based on the mice CSF are required.

Visual acuity (VA) is a simple yet commonly used metric for a first assessment of visual performance. VA is the smallest angular size a well-contrasted object, $|\gamma_M| = 1$, may have while being successfully detected/identified. It approximately corresponds to the

angular size associated to the maximum angular frequency f_0 for which the CSF is equal to unity, $C(f_0) = 1$. The rodent VA is very low in comparison with that of humans, being strongly limited by optical and neural factors (62). Estimates of behavioral rodent VA are fairly coincident across studies. Refs. 63–65 found values of f_0 close to 0.5 cycles per degree (cpd) for mice, while Long–Evans rats performed slightly better (1.0 cpd). For background luminance 60 cd m^{-2}, (66) found behavioral mice VA also equal
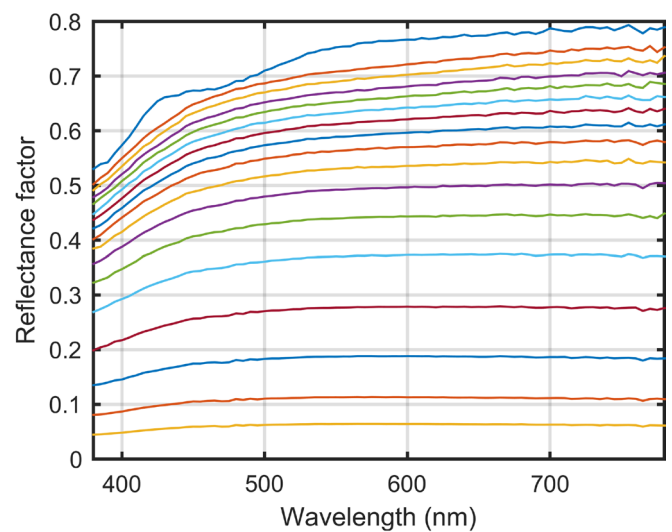

Fig. 3. Reflectance factor of the upper region of the ventral side of the barn owl specimen. Hyperspectral measurements were made under illumination normal to the frontal plane (source azimuth/altitude = 0°/0°). Different curves correspond to different observation angles within the sagittal plane, measured from the sagittal axis every 5°, from 0° *Top* line) to 85° (*Bottom* line).

to $f_0 = 0.5$ cpd. These behavioral VA are consistent with results obtained in optokinetic, optomotor, and visual evoked potential studies (most of them giving f_0 in the range 0.4 to 0.6 cpd for mice). In practical terms this means that an avian predator of size ~ 50 cm would appear visually unresolved by mice at a distance larger than ~ 30 m, and its flying silhouette would be discerned with resolution of 3×3 pixels or better only at a distance shorter than ~ 10 m.

VA nominally applies to highly contrasted objects. However, the absolute value of the Michelson contrast of barn owls against the moonlit sky is < 1. Furthermore, this contrast steadily decreases with distance due to two factors. On the one hand, the retinal image is the two-dimensional convolution of the ideal geometrical image and the eye's point spread function (63, 67) and, in consequence, unresolved retinal images have a nearly constant size, that of the PSF, independently from the true angular size of the object (68, 69). On the other hand, the corneal irradiance produced by the object steadily decreases with distance, following an inverse square law combined with atmospheric attenuation, also known as Allard's Law (70). Since the decreasing radiant flux entering the eye is spread over a constant-size retinal area, the relative contribution of the object against the (also blurred) background, and hence its contrast, is progressively smaller. This makes it necessary to analyze the quantitative CSFs, not just the VA, to estimate the maximum detection distance (see *SI Appendix*, Fig. S10 for estimates of the CSFs for M cones, S cones, and rods in mice).

The mice $C(f)$ estimated with the parameters provided above is conservative in the sense that it likely overestimates night-time mice behavioral sensitivity to predators in the upper visual field and the maximum distance at which mice may detect them (*SI Appendix*, Eq. S11). Two factors contribute to this overestimation: On the one hand, the ref. 71 contrast thresholds for S and M cones were determined for a background whose luminance (1.52 cd m^{-2}) was significantly higher than the luminance of the night sky (excepting in directions close to the Moon disc), so it could be expected that the actual thresholds in moonlit nights would be higher, and hence the CSFs lower. On the other hand, VA is higher in rats than in mice, so adopting the value $m = 2.88$ cpd^{-1} for cones and $m_{sc} = 3.27$ cpd^{-1} for rods based on ref. 72 measurements with hooded rats likely introduces some additional degree of overestimation in mice CSF.

In the S-cone band, the barn owl is always darker than the sky (Weber contrasts negative), regardless of the direction (*SI Appendix*, Fig. S11). Note however that the amount of environmental light is below the absolute radiance threshold of S-cones for all Moon altitudes, computed for a Moon phase −15° (close to full Moon), as well as for M-cones at the lowest altitude (20°). This means that these photoreceptors would not be active, and, in spite of the large contrast, a barn owl of size 15° would not be detected in the S-cone band. On the other hand, for the mid-altitude Moon (40° and 60°), there are wide regions of the sky in which the contrast in the active M-cone and rod bands lies within the invisibility range for objects of this size. Due to the continuity of the sky brightness distribution, the barn owl contrast becomes even 0 for a closed line of directions located between the labeled contours.

More distant (smaller) targets require larger contrast for detection (Fig. 4). The analysis of Denman contrast thresholds accounting for the variable angular size of the barn owl as a function of the distance to the prey indicates that the predator can approach the prey up to very short distances, in the range of a few meters, from a sizeable region of directions on the sky, especially in the M-cone and rod bands when the Moon is at mid-altitudes (Fig. 4).

An interesting issue is whether a darker ventral plumage will enable the barn owl to approach mice at such short distances without being detected. To address this question, we compared the expected detection distance for the actual (white) barn owl specimen compared to simulated "gray" darker morphs (Fig. 5). We found that the detection distance increases dramatically for gray simulated specimens, suggesting that they would be easier to detect by prey, triggering an early-warning signal that facilitates escape before the predator is too close.

Discussion

We have shown that the presence of the Moon on the night sky provides the necessary conditions for BM of avian predators as seen by their prey from the ground. For multiple Moon altitudes and combinations of spectral reflectance of the soil and the underparts of the predator, the contrast of the predator remains below the contrast detection threshold of prey and thus the predator becomes undetable to prey from a number of sky directions. This effect is enabled by the remarkably high Posch ratios (horizontal irradiance vs radiance of the sky in given directions) achievable when the Moon is above the horizon. Narrow-band BM can be achieved when the Posch ratio in a given direction of the sky equals π times the inverse of the product of soil and predator reflectance. Wide-band photoreceptor BM conditions also depend on the state of the atmosphere, on the spectral reflectance of the ground soil and the ventral side of the predators, and on the altitude of the Moon above the horizon, but they do not depend crucially on Moon phase, except for achieving the minimum level of environmental light required for eliciting photoreceptor responses (see below). The reason is that Moon phase mainly determines the overall extra-atmospheric irradiance on which both the numerator and the denominator of the Posch ratios are dependent. Its marginal effect on BM stems from the slightly different spectral composition of the moonlight reflected at different phases from the different regions of the Moon surface.

Both Moon phase and altitude are key factors determining the amount of environmental moonlight (73). Our calculations suggest that while the mouse rods are well above the absolute irradiance excitation threshold in all conditions, the M-cones are below it at all Moon altitudes for a substantial part of the lunar cycle (1/4 of total, from phase −45° to +45°), and the S-cones are below it for most altitudes and phases. Our results suggest that S-cones, for which even a white predator looks much darker than the surrounding sky, may afford rodents an efficient early warning pathway during twilight hours and daytime, when the ambient light is intense enough to keep them well within the mesopic or photopic range.

From our estimates of maximum detection distance, it seems that a white predator foraging in full-moon conditions may approach prey from a wide range of sky directions up within a few meters without being detected by the M-cones (slightly above absolute threshold) or rods (fully functional under moonlight). However, this critical benefit would not apply to darker predators, which may be detected at substantially larger distances. Differential detection distances depending on plumage color likely explain the fact that reddest barn-owls are less successful at hunting and providing food to their offspring during moonlit nights (24). Barn owls hunt rodents on the ground using two techniques, both implying flying above their prey: a) by diving down from a high perch –typically a tree branch, fence post, power pole, or a construction ledge–, and b) by a searching flight at 3 to 6 m above the ground with occasional hovering and a vertical drop down
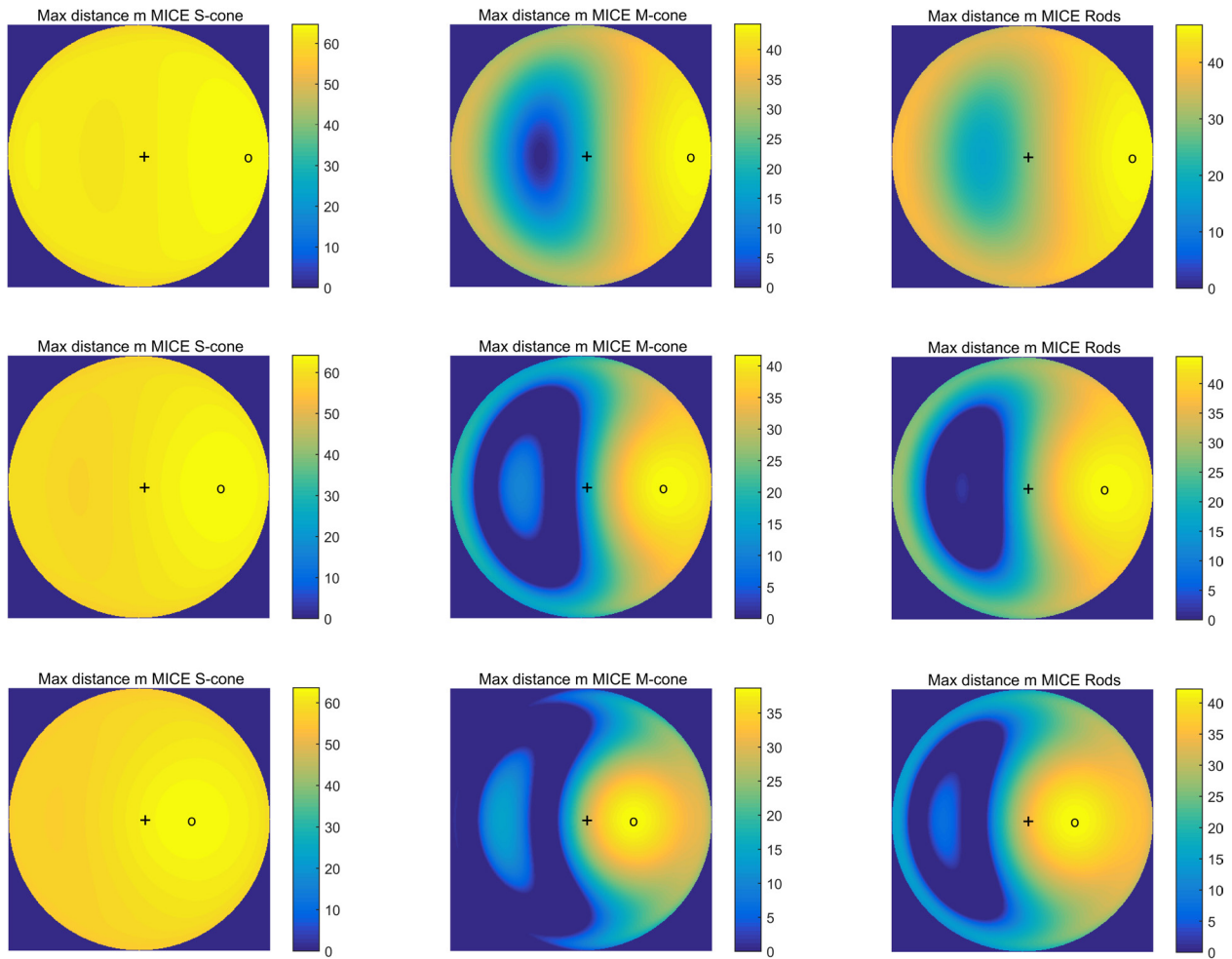
Fig. 4. Maximum distances (m) at which the barn owl can be detected in each photoreceptor band of mice, according to *SI Appendix*, Eq. (S11) and the parameters described in the text. The sky vault is projected onto a circle using a zenithal equal area projection. The avian predator transversal size is l = 50 cm. Moon and atmospheric parameters are the same as in *SI Appendix*, Fig. S11. This figure generalizes the information contained in the Denman contours of *SI Appendix*, Fig. S11, accounting for the variable angular size of the barn owl as a function of the distance to the prey. These panels can therefore be interpreted as the distances at which the barn owl can approach their prey from each sky direction while still being unnoticed by the corresponding mouse photoreceptor. Moon phase angle –15° (waxing gibbous Moon, illuminated fraction 98.3%). Atmosphere with aerosol optical depth 0.2, aerosol asymmetry parameter 0.6 and aerosol albedo 0.85. Rows, *Top to Bottom*: distances for Moon altitudes of 20°, 40°, and 60°, respectively. *Columns, Left to Right*: distances for the S-cones, M-cones, and rods, respectively. S-cone is always below its absolute irradiance threshold. Zenith is denoted with a + sign, Moon altitude is denoted as a circle. Color scales are specific for each subplot.

over the prey with the head first and a final strike with the talons (https://www.youtube.com/watch?v=FkP4Ro2gRl8&t=S2&ab_channel=BBCEarthUnplugged). In light of our results, a perpendicular angle of approach should confer adaptive significance on pale underparts –but not darker underparts– through concealment against the background sky. Differential effects of moonlight on nocturnal camouflage of different color morphs could result in performance trade-offs across moon altitudes above the horizon, with a marginal influence of the Moon phase. If this is true, we can expect phenotype–time correlations and signatures of selection on color morphs, as reported for barn owls (24). Nocturnal species could use time –as opposed to space– as a resource and adjust the timing of peak feeding activity and reproduction to match the moonlight conditions that maximize(s) their overall performance given their coloration, extending the process of matching habitat choice (*sensu* ref. 74) to a so far overlooked temporal dimension.

Given the isomorphic structure of the moonlit nightscapes and their corresponding daytime sunlit landscapes, our results can be applied to the study of camouflage by BM of diurnal species. Furthermore, our formal model includes the effects of fluorescent emission, observed in many taxa. Although not relevant for our

particular example of application and not discussed here, bioluminescence could also be incorporated to the general model developed in this paper.

This study has, none-the-less, several limitations. On the one hand, we have assumed for simplicity that ground reflections are Lambertian. We have also used an angularly averaged spectral reflectance for the predator's ventral surface, treating it as an equivalent Lambertian term. The actual bidirectional reflectance distribution functions of many natural surfaces, including diverse types of terrains and avian underparts, may show deviations from a perfect Lambertian behavior. However, the consequences of deviations from a perfectly Lambertian ground reflectance are attenuated when calculating the irradiance on the avian ventral surface and the corresponding radiance reflected from it (computational details omitted for brevity). For plumages that are not perfect Lambertian reflectors, the predator's contrast against the night sky could increase or decrease depending on each specific angle as the predator turns in flight, but this should not reduce the significance of BM as a form of nocturnal camouflage, since perfect concealment in all circumstances is not required for this mechanism to make a significant contribution to the overall foraging success and fitness of nocturnal predators. The measurements of the spectral
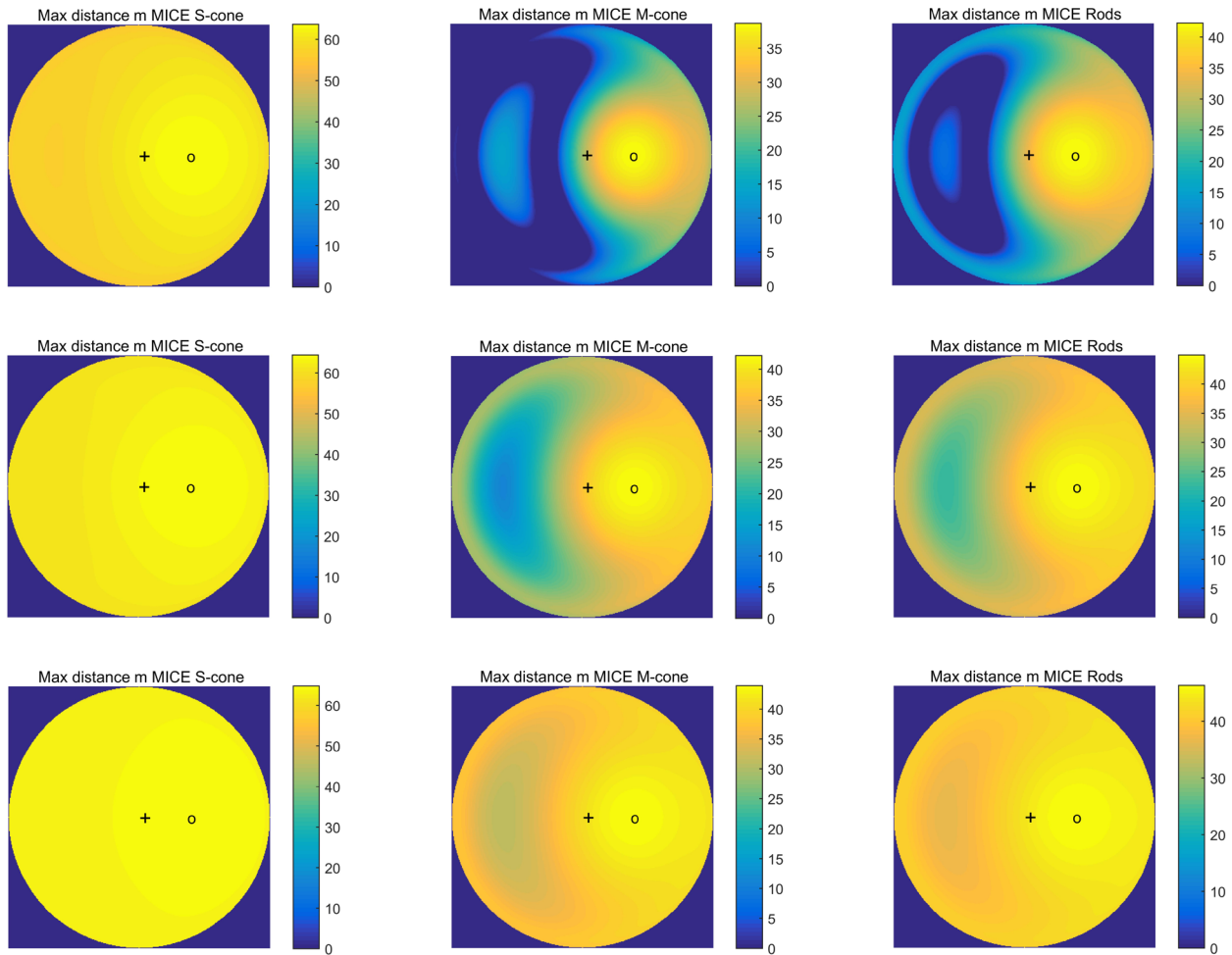
Fig. 5. Maximum detection distances (m) of the original white barn owl *Top* row and of two simulated gray versions, one with 50% (*Middle* row) and other with 25% (*Bottom* row) of the original barn owl reflectance. Columns, *Left to Right*: distances for the S-cones, M-cones, and rods, respectively. All plots correspond to a Moon altitude 60° and phase angle –15°, with the same atmospheric parameters as in *SI Appendix*, Fig. S11. The *Middle* and *Bottom* rows show that barn owls with simulated gray plumages could be detected against the sky background from much larger distances than white ones. S-cone is always below its absolute irradiance threshold. Zenith is denoted with a + sign, Moon altitude as a circle. Color scales are specific for each subplot.

reflectance of barn owls are not available below 300 nm, missing a small part of the S-cone detection bandpass, something we addressed with a cautious extrapolation toward shorter wavelengths. The measurements of the fluorescent response of our barn owl specimen ventral plumage are limited in spectral extent. An intriguing issue is whether the more intense fluorescent emission expected from living barn owls could provide enough radiance in the mouse S-cone band to significantly decrease the contrast and, in consequence, the expected detection distance, something that deserves further studies.

The atmospheric scattering model used in this study encompasses only first-order scattering of moonlight photons, neglecting second- and higher-order scattering events. This may lead to some underestimation of the sky radiance at low altitudes above the horizon. Also, we did not address here the effects related to the polarization state of the direct, scattered, and reflected light.

We have quantified the radiance contrast within each photoreceptor of the potential prey. In this work, we do not report chromatic contrast or the coordinates of each luminous stimulus in the dichromatic mice color space. Note that zero Weber contrast in all photoreceptors would grant equal color coordinates, but equal color could in principle be also achieved even if that condition is not fulfilled. How circadian regulation modulates threat

avoidance performance of prey throughout the night remains an open question. Interestingly, mice behavioral responses show higher sensitivity to light at night, compared with daytime (75)

We have assumed clear, cloudless skies. The presence of clouds in pristine natural environments free from artificial light pollution would just modify the radiance distribution across the sky, with variable effects regarding the average radiance and its angular anisotropy. Such variability can be accounted for in the Ψ function, either in a deterministic or a stochastic sense, and as such they do not affect the basic isomorphism between day and night landscapes. They may of course modify the feasibility of achieving BM under moon or sunlight, but as long as the light source is fully or partially visible through the clouds, the essential conclusions of this work remain applicable. Still, a detailed analysis of these effects remains to be done.

The BM effect under clear moonlit (or sunlit) skies described by this model is overall robust to modifications of various model parameters, even though the details of the outputs (e.g. the detection distance all-sky maps) do change in response to smooth changes in the inputs. BM effects are robust against changes in the state of the atmosphere (aerosol optical depth and asymmetry parameter; see *SI Appendix*, Figs. S3A, S5 and S13), illuminant geometry and brightness (Moon altitude, Fig. 4, and phase; see
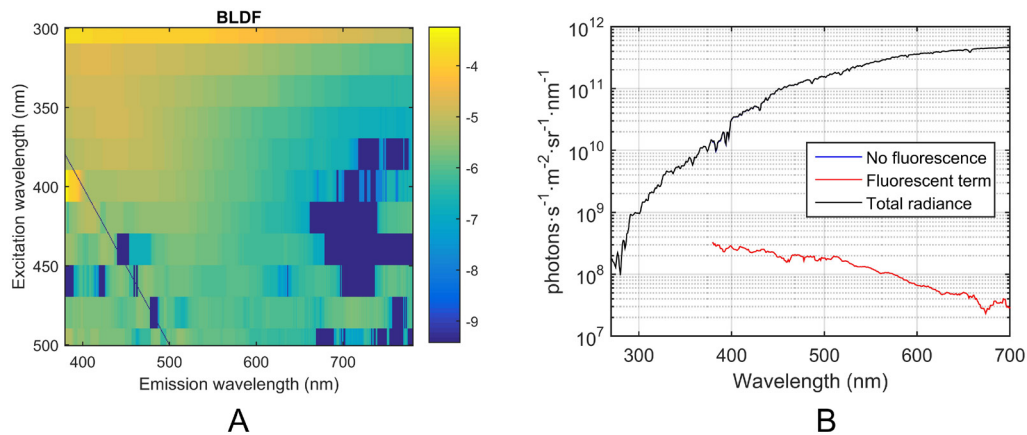
Fig. 6. (*A*) BLDF of the upper region of the ventral side of the barn owl specimen for excitation wavelengths in the range 300 to 500 nm and observation in the range 380 to 780 nm. Log$_{10}$(sr^{-1}) scale. (*B*) Ventral spectral radiance of the barn owl under illumination reflected from ground, with the Moon at altitude 60° and phase –15° in an atmosphere with AOD = 0.2 and aerosol asymmetry parameter 0.6. In case of our specimen, the fluorescent radiance (red curve) was several orders of magnitude smaller than the non-fluorescent one, such that the resulting spectral radiance is for all practical purposes the latter (black curve).

SI Appendix, Fig S3*B*), predator reflectance (Fig. 5), and soil reflectance (*SI Appendix*, Figs. S12 and S13). Of course, this does not mean that the BM mechanism is effective in all circumstances: In some cases, the predicted detection distance may be large enough for the prey to escape to safety before being captured. Optimal functioning of this BM mechanism is also not expected before the Moon rises or in completely overcast skies. Hence, situations where BM is possible are by no means exceptional, but rather common whenever the Moon is above the horizon.

Future field validation of the model in this and other nocturnal predator–prey systems (e.g. nightjar-moth) is required. For this, observations of the flight paths of attacking predators may be collected (e.g. using biologging devices or animal-borne cameras) and analyzed to test for the expected increase in hunting efficiency when predators approach prey from low contrast directions. Finally, light pollution is an increasingly relevant and global contributor to environmental light (76, 77) and its ecological effects cannot be ignored (78–80). Partially cloudy or overcast skies can amplify the effects of artificial light (81–83). In particular, light pollution is very efficient at erasing the moonlight signature across the sky (84), with documented effects on the sky Posch ratios in terrestrial and marine environments (27, 29). The effects on BM of the artificial diffuse skyglow, as well as those produced by nearby direct light sources in artificially lit environments, is the subject of ongoing work.

Material and Methods

A set of measurements of three basic optical properties were taken from a male specimen of barn owl that conformed to the typical white morph of the species, as opposed to the dark reddish morph and the patterned plumage of all other owl species (specimen EBD 33015A from the Scientific Collection of the Estación Biológica de Doñana-CSIC (ICTS-Doñana); see ref. 24 for pictures of contrasting color morphs of the barn owl): i) the spectral BRDF of the owl for different geometries of illumination and observation, ii) the general shape of the spectral reflectance in the UV-A wavelengths within the S-cone band of mice, and iii) the BLDF describing the fluorescent re-emission of barn owl feathers.

The hyperspectral BRDF measurements were carried out at the Color Imaging Lab in the Optics Department, Science Faculty at the University of Granada, Spain. The capture device used for the BRDF measurement in the VIS/NIR range (from 397 to 1004 nm) was a SPECIM-IQ hyperspectral camera [www.specim.com] based on a CMOS sensor with 512 × 512 pixels spatial resolution, with 204 different spectral channels. For each image, we recorded

a raw capture of the scene and a raw capture of a reference white sample (20 × 20-cm barium sulfate tile by Sphere Optics) as well as a dark image. All three images were acquired using the same capturing parameters such as exposure time, ISO gain, focusing, and framing. With this information, the spectral reflectance image was then calculated by correcting each pixel of the raw image by applying a flat field correction:

$$R(\lambda, x, y) = \left[\frac{S(\lambda, x, y) - D(\lambda, x, y)}{W(\lambda, x, y) - D(\lambda, x, y)} \right] R_{\text{ref}}(\lambda). \quad \textbf{[7]}$$

Where $R(\lambda, x, y)$ is the corrected spectral reflectance image, $S(\lambda, x, y)$ is the raw image of the sample, $D(\lambda, x, y)$ is the raw dark image, $W(\lambda, x, y)$ is the raw image of the reference white tile, $R_{\text{ref}}(\lambda)$ is the known spectral reflectance of the reference white tile (assumed spatially homogeneous all across it), λ stands for wavelength and (x, y) are the spatial coordinates of each pixel.

The spectral reflectance in the near UV 300 to 380 nm, spectral BRDF 680 to 780 nm, and BLDF for 300 to 500 nm excitation and 380 to 780 nm re-emission wavelengths, were measured at the laboratory of GIMRO-CSIC in Madrid. The measuring system is a gonispectrophotometer with SI-traceability, especially developed for measuring BRDF. The relative expanded uncertainty for the kind of samples evaluated in the article is around 1%. Detailed information on this system is given in refs. 85 and 86.

For the calculations of the predator contrast against the moonlit sky we used a solid-angle weighted average of the spectral BRDFs in Fig. 3, assuming rotational symmetry around the sagittal axis (*SI Appendix,* Fig. S6 "Ventral"). The angularly averaged BRDFs were linearly extrapolated below 380 nm to cover the 300 to 380 nm range (Fig. 1 "Ventral extrap"). The corresponding Lambertian reflectance factor of the owl ventral side, ρ_a^-, is then obtained as the angularly averaged BRDF multiplied by π.

The fluorescent properties of the plumage were measured under successive monochromatic illumination with eleven excitation wavelengths, every 20 nm from 300 nm to 500 nm, recording the emission spectrum across the 380 to 780 nm range. From the measured emission spectra, the corresponding BLDFs were calculated. They are displayed as a Donaldson matrix in log10 scale in Fig. 6*A*. The BLDFs were subsequently interpolated with a 1 nm step both over excitation and emission wavelengths.

Data, Materials, and Software Availability. Code data have been deposited in Zenodo (https://doi.org/10.5281/zenodo.12701820) (87). All other data are included in the manuscript and/or *SI Appendix*.

Author affiliations: [a]Estación Biológica de Doñana, Department of Ecology and Evolution, Consejo Superior de Investigaciones Científicas (CSIC), Sevilla E-41092, Spain; [b]Independent scholar Former Profesor Titular de Universidade (retired) at Universidade de Santiago de Compostela (USC), Facultade de Óptica e Optometría, Santiago de Compostela E-15782, Galicia; [c]Departamento de Física, Universidad de Córdoba, Córdoba E-14071, Spain; [d]Departamento de Óptica, Universidad de Granada (UGR), Granada E-18071, Spain; [e]Instituto de Óptica "Daza de Valdés", Consejo Superior de Investigaciones Científicas (CSIC), Madrid E-28006, Spain; [f]Photonics4Life Research Group, Departamento de Física Aplicada, Facultade de Física e Facultade de Óptica e Optometría, Instituto de Materiais (iMATUS), Universidade de Santiago de Compostela, Santiago de Compostela E-15782, Spain; [g]Institut de Ciències del Cosmos (ICCUB), Universitat de Barcelona (UB), Barcelona E-08028, Spain; [h]Departament de Física Quàntica i Astrofísica (FQA), Universitat de Barcelona (UB), Barcelona E-08028, Spain; and [i]Institut d'Estudis Espacials de Catalunya (IEEC), Castelldefels (Barcelona) E-08860, Spain

1. G. H. Thayer, *Concealing-coloration in the Animal Kingdom* (Macmillan, New York, 1909), pp. 72.
2. H. B. Cott, *Adaptive Coloration in Animals* (Metheun, London, 1940).
3. M. Koneru, T. Caro, Animal coloration in the Anthropocene. *Front. Ecol. Evol.* **10**, 857317 (2022).
4. J. J. Negro, J. H. Sarasola, F. Fariñas, I. Zorrilla, Function and occurrence of facial flushing in birds. *Comp. Biochem. Physiol. A* **143**, 78–84 (2006).
5. J. J. Negro et al., Contrasting stripes are a widespread feature of group living in birds, mammals and fishes. *Proc. R. Soc. B* **287**, 20202021 (2020).
6. I. Galván, D. Palacios, J. J. Negro, The bare head of the Northern bald ibis (Geronticus eremita) fulfills a thermoregulatory function. *Front. Zool.* **14**, 1–9 (2017).
7. M. Stevens, S. Merilaita, Animal camouflage: Current issues and new perspectives. *Phil. Trans. R. Soc. B* **364**, 423–427 (2009).
8. W. L. Allen, R. Baddeley, I. C. Cuthill, N. E. Scott-Samuel, A quantitative test of the predicted relationship between countershading and lighting environment. *Am. Nat.* **180**, 762–776 (2012).
9. S. Johnsen, Cryptic and conspicuous coloration in the pelagic environment. *Proc. Biol. Sci.* **269**, 243–256 (2002).
10. J. L. Kelley, I. Taylor, N. S. Hart, J. C. Partridge, Aquatic prey use countershading camouflage to match the visual background. *Behav. Ecol.* **28**, 1314–1322 (2017).
11. R. A. Kiltie, Countershading: Universally deceptive or deceptively universal? *Trends Ecol. Evol.* **3**, 21–23 (1988).
12. M. Kocifaj, Sky luminance/radiance model with multiple scattering effect. *Solar Energy* **83**, 1914–1922 (2009).
13. M. Kocifaj, Blurring the boundaries between Standard General Sky types due to multiple scattering of light. *Lighting Res. Technol.* **45**, 485–494 (2013).
14. M. Kocifaj, L. Kómar, Physics interpretation of ISO/CIE sky types. *Solar Energy* **225**, 3–10 (2021).
15. M. Kocifaj, B. Kránicz, Modelling clear sky colours: A single scattering approach. *Lighting Res. Technol.* **43**, 497–512 (2011).
16. D. E. Nilsson, J. Smolka, Quantifying biologically essential aspects of environmental light. *J. R. Soc. Interface* **18**, 20210184 (2021).
17. D. E. Nilsson, J. Smolka, M. Bok, The vertical light-gradient and its potential impact on animal distribution and behavior. *Front. Ecol. Evol.* **10**, 951328 (2022).
18. I. C. Cuthill et al., Optimizing countershading camouflage. *Proc. Natl. Acad. Sci.* **113**, 13093–13097 (2016).
19. T. Morimoto, S. Kishigami, J. M. M. Linhares, S. M. C. Nascimento, H. E. Smithson, Hyperspectral environmental illumination maps: Characterizing directional spectral variation in natural environments. *Opt. Express* **27**, 32277–32293 (2019).
20. O. Penacchio et al., Three-dimensional camouflage: Exploiting photons to conceal form. *Am. Nat.* **186**, 553–563 (2015).
21. R. Séchaud et al., Behaviour-specific habitat selection patterns of breeding barn owls. *Mov. Ecol.* **9**, 1–11 (2021).
22. J. Del Hoyo, A. Elliott, J. Sargatal, Eds., *Handbook of the Birds of the World (Barn-owls to Hummingbirds.* **5**, (Lynx Edicions, Barcelona, 1999).
23. A. Roulin, J. Mangels, K. Wakamatsu, T. Bachmann, Sexually dimorphic melanin-based colour polymorphism, feather melanin content, and wing feather structure in the barn owl (Tyto alba). *Biol. J. Linn. Soc.* **109**, 562–573 (2013).
24. L. M. San Jose et al., Differential fitness effects of moonlight on plumage colour morphs in barn owls. *Nat. Ecol. Evol.* **3**, 1331–1340 (2019).
25. G. Beauchamp, P. Heeb, Social foraging and the evolution of white plumage. *Evol. Ecol. Res.* **3**, 703–720 (2001).
26. H. Wagner, M. Weger, M. Klaas, W. Schröder, Features of owl wings that promote silent flight. *Interface Focus* **7**, 20160078 (2017).
27. S. Bará, X. Pérez-Couto, F. Falchi, M. Kocifaj, E. Masana, Estimating linear radiance indicators from the zenith night-sky brightness: On the Posch ratio for natural and light-polluted skies. *Mon. Not. R. Astron. Soc.* **512**, 2125–2134 (2022).
28. A. Jechow, C. C. M. Kyba, F. Hölker, Mapping the brightness and color of urban to rural skyglow with all-sky photometry. *J. Quant. Spectrosc. Radiat. Transf.* **250**, 106988 (2020).
29. X. Pérez-Couto, F. Falchi, S. Bará, On the Posch ratio for irradiance in coastal waters and the high seas. *J. Quant. Spectrosc. Radiat. Transf.* **298**, 108503 (2023).
30. G. D. Field, A. P. Sampath, Behavioural and physiological limits to vision in mammals. *Phil. Trans. R. Soc. B* **372**, 20160072 (2017).
31. R. T. Hanlon et al., Adaptable night camouflage by cuttlefish. *Am. Nat.* **169**, 543–551 (2007).
32. A. Kelber, C. Yovanovich, P. Olsson, Thresholds and noise limitations of colour vision in dim light. *Phil. Trans. R. Soc. B* **372**, 20160065 (2017).
33. D. C. O'Carroll, E. J. Warrant, Vision in dim light: Highlights and challenges. *Phil. Trans. R. Soc. B* **372**, 20160062 (2017).
34. V. Penteriani, M. M. Delgado, Living in the dark does not mean a blind life: Bird and mammal visual communication in dim light. *Phil. Trans. R. Soc. B* **372**, 20160064 (2017).
35. E. Masana, J. M. Carrasco, S. Bará, S. J. Ribas, A multi-band map of the natural night sky brightness including Gaia and Hipparcos integrated starlight. *Mon. Not. R. Astron. Soc.* **501**, 5443–5456 (2021).
36. E. Masana, S. Bará, J. M. Carrasco, S. J. Ribas, An enhanced version of the Gaia map of the brightness of the natural sky. *Int. J. Sustain. Lighting.* **24**, 1–12 (2022).
37. H. H. Kieffer, T. C. Stone, The spectral irradiance of the Moon. *Astron. J.* **129**, 2887–2901 (2005).
38. R. C. Bohlin, K. D. Gordon, P.-E. Tremblay, Techniques and review of absolute flux calibration from the ultraviolet to the mid-infrared. *Pub. Astr. Soc. Pac.* **126**, 711–732 (2014).
39. Space Telescope Science Institute (STScI), CALSPEC, https://www.stsci.edu/hst/instrumentation/reference-data-for-calibration-and-tools/astronomical-catalogs/calspec. Accessed 7 July 2023.
40. Bureau International des Poids et Mesures (BIPM), *Le Système International d'unités/The International System of Units* (BIPM, Sèvres, France, ed. 9, 2019).
41. A. Jones, S. Noll, W. Kausch, C. Szyszka, S. Kimeswenger, An advanced scattered moonlight model for Cerro Paranal. *A&A* **560**, A91 (2013).
42. Y. I. Velikodsky et al., New Earth-based absolute photometry of the Moon. *Icarus* **214**, 30–45 (2011).
43. R. Román et al., Correction of a lunar-irradiance model for aerosol optical depth retrieval and comparison with a star photometer. *Atmos. Meas. Tech.* **13**, 6293–6310 (2020).
44. F. Kasten, A. T. Young, Revised optical air mass tables and approximation formula. *Appl. Opt.* **28**, 4735–4738 (1989).
45. P. M. Teillet, Rayleigh optical depth comparisons from various sources. *Appl. Opt.* **29**, 1897–1900 (1990).
46. A. McComiskey et al., Direct aerosol forcing: Calculation from observables and sensitivities to inputs. *J. Geophys. Res.* **113**, D09202 (2008).
47. J. Dunning et al., How woodcocks produce the most brilliant white plumage patches among the birds. *J. R. Soc. Interface* **20**, 20220920 (2023).
48. V. Penteriani, M. M. Delgado, C. Alonso-Alvarez, F. Sergio, The importance of visual cues for nocturnal species: Eagle owls signal by badge brightness. *Behav. Ecol.* **18**, 143–147 (2007).
49. Y. Fu, K. W. Yau, Phototransduction in mouse rods and cones. *Pflugers Arch.* **454**, 805–819 (2007).
50. I. Rhim, G. Coello-Reyes, I. Nauhaus, Variations in photoreceptor throughput to mouse visual cortex and the unique effects on tuning. *Sci. Rep.* **11**, 11937 (2021).
51. F. M. Nadal-Nicolás et al., True S-cones are concentrated in the ventral mouse retina and wired for color detection in the upper visual field. *eLife* **9**, e56840 (2020).
52. K. P. Szatko et al., Neural circuits in the mouse retina support color vision in the upper visual field. *Nat. Commun.* **11**, 3481 (2020).
53. A. Hughes, "The topography of vision in mammals of contrasting life style: Comparative optics and retinal organisation" in *Handbook of Sensory Physiology VII/5*, F. Crescitelli, Ed. (Springer, Berlin, 1977), pp. 613–756.
54. A. Hughes, A schematic eye for the rat. *Vision Res.* **19**, 569–588 (1979).
55. D. J. Wallace et al., Rats maintain an overhead binocular field at the expense of constant fusion. *Nature* **498**, 65–69 (2013).
56. M. F. Land, Animal vision: Rats watch the sky. *Curr. Biol.* **23**, R611–R613 (2013).
57. J. M. Hayes, G. W. Balkema, Elevated dark-adapted thresholds in hypopigmented mice measured with a water maze screening apparatus. *Behav. Genet.* **23**, 395–403 (1993).
58. S. Bará, M. Martin Aubé, J. Barentine, J. Zamorano, Magnitude to luminance conversions and visual brightness of the night sky. *Mon. Not. R. Astron. Soc.* **493**, 2429–2437 (2020).
59. M. Kocifaj, F. Kundracik, J. C. Barentine, S. Bará, The proliferation of space objects is a rapidly increasing source of artificial night sky brightness. *Mon. Not. R. Astron. Soc. Lett.* **504**, L40–L44 (2021).
60. N. M. Alam, C. M. Altimus, R. M. Douglas, S. Hattar, G. T. Prusky, Photoreceptor regulation of spatial visual behavior. *Invest. Ophthalmol. Vis. Sci.* **56**, 1842–1849 (2015).
61. Y. Umino, E. Solessio, R. B. Barlow, Speed, spatial, and temporal tuning of rod and cone vision in mouse. *J. Neurosci.* **28**, 189–198 (2008).
62. P. Artal, P. Herreros de Tejada, C. Muñoz Tedó, G. D. Green, Retinal image quality in the rodent eye. *Vis. Neurosci.* **15**, 597–605 (1998).
63. G. T. Prusky, P. W. West, R. M. Douglas, Behavioral assessment of visual acuity in mice and rats. *Vision Res.* **40**, 2201–2209 (2000).
64. G. T. Prusky, N. M. Alam, S. Beekman, R. M. Douglas, Rapid quantification of adult and developing mouse spatial vision using a virtual optomotor system. *Invest. Ophthalmol. Vis. Sci.* **45**, 4611–4616 (2004).
65. G. T. Prusky, R. M. Douglas, Characterization of mouse cortical spatial vision. *Vision Res.* **44**, 3411–3418 (2004).
66. M. H. Histed, L. A. Carvalho, J. H. Maunsell, Psychophysical measurement of contrast sensitivity in the behaving mouse. *J. Neurophysiol.* **107**, 758–765 (2012).
67. J. W. Goodman, *Introduction to Fourier Optics* (McGraw-Hill, New York, NY, ed. 2, 1996), p. 134.
68. S. Bará, R. C. Lima, Quantifying the visual impact of wind farm lights on the nocturnal landscape. arXiv [Preprint] (2024). (accesed 15 July 2024).), https://arxiv.org/pdf/2310.05981.
69. R. Navarro, M. A. Losada, Shape of stars and optical quality of the human eye. *J. Opt. Soc. Am. A* **14**, 353–359 (1997).
70. É. Allard, *Mémoire sur l'intensité et la portée des phares* (Imprimerie Nationale Paris, 1876), pp. 74–75.
71. D. J. Denman et al., Mouse color and wavelength-specific luminance contrast sensitivity are non-uniform across visual space. *eLife* **7**, e31209 (2018).
72. D. Birch, G. H. Jacobs, Spatial contrast sensitivity in albino and pigmented rats. *Vision Res.* **19**, 933–937 (1979).
73. C. C. M. Kyba, J. Conrad, T. Shatwell, Lunar illuminated fraction is a poor proxy for moonlight exposure. *Nat. Ecol. Evol.* **4**, 318–319 (2020).

74. P. Edelaar, A. M. Siepielski, J. Clobert, Matching habitat choice causes directed gene flow: A neglected dimension in evolution and ecology. *Evolution* **62**, 2462–2472 (2008).
75. S. Koskela, T. Turunen, P. Ala-Laurila, Mice reach higher visual sensitivity at night by using a more efficient behavioral strategy. *Curr. Biol.* **30**, 42–53 (2020).
76. F. Falchi *et al.*, The new world atlas of artificial night sky brightness. *Sci. Adv.* **2**, e1600377 (2016).
77. A. Sánchez de Miguel, J. Bennie, E. Rosenfeld, S. Dzurjak, K. J. Gaston, First estimation of global trends in nocturnal power emissions reveals acceleration of light pollution. *Remote Sens.* **13**, 3311 (2021).
78. J. Bennie, J. P. Duffy, T. W. Davies, M. E. Correa-Cano, K. J. Gaston, Global trends in exposure to light pollution in natural terrestrial ecosystems. *Remote Sens.* **7**, 2715–2730 (2015).
79. T. Longcore *et al.*, Rapid assessment of lamp spectrum to quantify ecological effects of light at night. *J. Exp. Zool.* **329**, 511–521 (2018).
80. O. McMahon, T. Smyth, T. W. Davies, Broad spectrum artificial light at night increases the conspicuousness of camouflaged prey. *J. Appl. Ecol.* **59**, 1324–1333 (2022).
81. C. C. M. Kyba, T. Ruhtz, J. Fischer, F. Hölker, Red is the new black: How the colour of urban skyglow varies with cloud cover. *Mon. Not. R. Astron. Soc.* **425**, 701–708 (2012).
82. S. J. Ribas, J. Torra, F. Figueras, S. Paricio, R. Canal-Domingo, How Clouds are Amplifying (or not) the Effects of ALAN. *Int. J. Sustain. Lighting* **35**, 32–39 (2016).
83. S. J. van Hasselt *et al.*, Cloud cover amplifies the sleep-suppressing effect of artificial light at night in geese. *Environ. Pollut.* **273**, 116444 (2021).
84. S. Bará, Anthropogenic disruption of the night sky darkness in urban and rural areas. *R. Soc. Open Sci.* **3**, 160541 (2016).
85. A. M. Rabal *et al.*, Automatic gonio-spectrophotometer for the absolute measurement of the spectral BRDF at in- and out-of-plane and retroreflection geometries. *Metrologia* **49**, 213 (2012).
86. B. Bernad, A. Ferrero, A. Pons, M. L. Herranz, J. Campos, Upgrade of goniospectrophotometer GEFE for near-field scattering and fluorescence radiance measurements. *Proc. SPIE* **9398**, 93980E (2015).
87. S. Bará, Background Matching against the moonlit night sky (Matlab code). Zenodo. https://doi.org/10.5281/zenodo.12701820. Deposited 9 July 2024.